MICROSTRUCTURE, TOUGHNESS CURVES AND MECHANICAL PROPERTIES OF ALUMINA CERAMICS

STEPHEN J. BENNISON, JÜRGEN RÖDEL, SRINIVASARAO LATHABAI,
PRAPAIPAN CHANTIKUL, BRIAN R. LAWN
Ceramics Division
National Institute of Standards and Technology
Gaithersburg, MD 20899, USA

ABSTRACT. The microstructural variables that determine the toughness (T-curve) characteristics of alumina and other structural ceramics are considered. Alumina ceramics gain their toughness from shielding by grain-interlock bridging at the interface behind the crack tip. A general fracture mechanics formalism for describing the bridging is outlined in terms of desirable microstructural elements, such as weak internal boundaries, high internal stress, coarse microstructure. The T-curve imparts the quality of flaw tolerance to the strength properties. We examine this quality, under both inert and interactive environmental conditions, monotonic and cyclic loading, using indentation flaws. In situ observations of bridging sites during loading in the scanning electron microscope provide insight into the bridge degradation micromechanisms. Finally, short-crack properties, spontaneous microcracking and wear degradation, are examined in light of the bridging model. It is concluded that design with ceramics may require certain tradeoffs, long vs short cracks, high strength vs flaw tolerance, etc. The key to optimal performance in ceramics rests with microstructural processing for specific properties.

1. INTRODUCTION

It is now well established that many monophase ceramics exhibit the property of rising fracture resistance or toughness with crack extension (R-curve or T-curve) [1-14]. The magnitude of the toughness increase can be respectable, in extreme cases approaching a factor of five or so over extensions of several millimeters or hundreds of grain dimensions.

Toughness-curve characteristics dictate mechanical behavior. For example, the associated stabilizing effect on crack growth confers the

209

quality of "damage tolerance" [5,9,12-14], i.e. insensitivity of strength to flaw size. This leads to the highly appealing prospect of a well-defined, flaw-insensitive stress for engineering design. However, the cost of gaining flaw tolerance is inevitably the sacrifice of toughness in the domain of "short" cracks, where properties like wear resistance are decided. Specifying the T-curve for optimal performance of ceramics involves certain tradeoffs.

A substantial body of evidence now exists to demonstrate that the principal mechanism of T-curve behavior in alumina and other ceramics is grain-localized bridging at the crack interface behind the advancing tip [1-14]. Bridging grains exert frictional closure forces across the crack walls and thereby shield the tip from the applied stress-intensity field [8,9,13,14]. The cumulation of bridging tractions over the crack interface with continued propagation leads to a rising toughness curve.

The magnitude and shape of the resultant T-curve are sensitive to the microstructure: grain size and shape [4,5,13,15]; internal residual stresses (e.g. thermal expansion anisotropy) in noncubic materials [13], especially as they may be intensified by incorporation of a second phase [16]; grain boundary energy [13]; all these are important players in the toughness. This strong influence of microstructure leads to the potential for manipulation of crack-resistance properties through controlled processing. Opportunities for the development of improved structural ceramics thereby rest with the development of novel microstructures and fabrication strategies that exploit the operative toughening micromechanisms.

In the present paper we review the toughness-curve phenomenon in ceramics, with alumina as a model system. First a microstructure-based model for grain bridging is discussed. Second, we examine the role of the T-curve in determining different mechanical properties. Primary consideration is given to strength properties [9,12,13,15,17,18], in both inert and interactive environments, and under quasistatic and (cyclic) fatigue loading. This is the domain of "intermediate" crack sizes (corresponding to the rising portion of the T-curve). Additional consideration is given to microfracture-induced wear properties [19], the domain of "short" cracks. Noting further that most conventional toughness evaluations are made in specimens with "long" cracks, we emphasize the importance of identifying any specific mechanical property with the proper crack-size domain. Then we present results of more recent, in situ observations of grain bridging in the scanning electron microscope [20]. Measurements of crack profiles demonstrate directly the nature of the closure forces exerted by the bridges on the cracks, and reveal details of fatigue processes. Finally, the prospects of innovative microstructural processing for optimizing toughness properties of ceramics, including composite systems, is discussed.

2. MICROSTRUCTURAL FRACTURE MECHANICS MODEL

2.1   GENERAL EQUILIBRIUM REQUIREMENTS

Begin by defining a net **crack-tip** stress-intensity factor condition for a crack subject to a superposed tensile loading field, $K_a(c)$, flaw-localized residual nucleation field, $K_r(c)$, and microstructure-associated field, $K_\mu(c)$ [14]:

$$K_*(c) = K_a(c) + K_r(c) + K_\mu(c).$$ (1)

Equilibrium obtains when K_* just balances the intrinsic toughness associated with the creation of crack surfaces:

$$K_* = T_0.$$ (2)

This last requirement can be restated by considering K_a and K_r in Eq. 1 as part of the net effective applied mechanical field, K_A, and $K_\mu = -T_\mu$ as part of the internal toughness, i.e.

$$\begin{aligned} K_A(c) &= K_a(c) + K_r(c) \\ &= T_0 + T_\mu(c) = T(c). \end{aligned}$$ (3)

The net **toughness** function $T(c)$ constitutes the so-called T-curve, the K-field equivalent of the R-curve.

An alternative formulation for the crack-tip conditions may be given in terms of the mechanical-energy-release rates [14]. Write, in analogy to Eq. (3),

$$G_A(c) = R_0 + R_\mu(c) = R(c)$$ (4)

with R the crack-resistance energy. The Griffith requirement for equilibrium is then

$$G_* = R_0 = 2\gamma_B$$ (5)

where γ_B is the fracture surface energy of the body in inert atmospheres. For intergranular fracture γ_B incorporates the grain boundary energy. By defining the connecting relations [14]

$$K_A = (G_A E')^{1/2}$$ (6a)
$$K_* = (G_* E')^{1/2}$$ (6b)

with $E' = E/(1 - \nu^2)$ in plane strain, E Young's modulus and ν Poisson's ratio, we identify the intrinsic toughness $T_0 = (R_0 E')^{1/2}$ in Eq. 2.

2.2   MICROSTRUCTURAL STRESS-INTENSITY FACTOR

Microstructural properties are introduced into the formalism in Sect. 2.1 via $T_\mu(c)$ in Eq. 3. For materials that toughen by bridging we need to determine the micromechanics of grain interlock and subsequent pullout [13]. A subsidiary element of the process is the segmentation of the primary crack front at incipient bridging grains, driven by conflicting tendencies to follow weak intergranular or interphase boundaries and local thermal expansion anisotropy tensile stresses. For the present we focus on simplistic, idealized structures in monophase, noncubic ceramics.

Consider a **half-penny** crack, radius c, evolving in a rectangular microstructure, Fig. 1. The submicroscopic crack is assumed to begin its life as a flaw in a region of most favorable internal **tension**, $+\sigma_R$, and thereafter to intersect bridging grains as it expands radially outward. The grains which act as bridges are assumed to be those with **compressive** components of the residual stress field, $-\sigma_R$, at transverse facets. The problem is then to determine the closure stresses exerted by the bridges in terms of crack-wall separation.

These stresses are governed by Coulombic friction that restricts the separation of bridging grain facets. At initial separation the bridging grains debond along the constrained facets and then "pull out" until final "rupture" at some critical rupture strain. The debond stage consumes relatively little energy, so the constitutive relation between closure stress p and (half-) crack-opening displacement u for a single bridge may be written exclusively in terms of a simple tail-dominated pullout relation [8,13]:

$$p(u) = p_M(1 - u/u_\ell) \qquad (7)$$

where p_M is the maximum resistance stress (at $u = 0$) and u_ℓ is the wall-wall half-displacement at bridge-matrix disengagement (at $p = 0$). The essential material quantities in Eq. 7 are contained in the parameters [13]:

$$u_\ell = \epsilon_\ell \ell/2 \qquad (8a)$$
$$p_M = (\alpha_\lambda \alpha_L \epsilon_\ell \mu \sigma_R)(1 - 1/2\alpha_d^2) \qquad (8b)$$

with ℓ grain size, μ friction coefficient, σ_R internal residual stress. The α and ϵ terms are dimensionless constants for geometrically similar microstructures:

$$\alpha_\lambda = \lambda/\ell \qquad (9a)$$
$$\alpha_L = L/\ell \qquad (9b)$$
$$\alpha_d = d/\ell \qquad (9c)$$
$$\epsilon_\ell = 2u_\ell/\ell \qquad (9d)$$

with λ the bridge cross-sectional perimeter, L the embedded grain length, d the bridge spacing. In Eq. 8 only the pullout distance u_ℓ depends on the grain size; the closure stress p_M is scale-invariant.
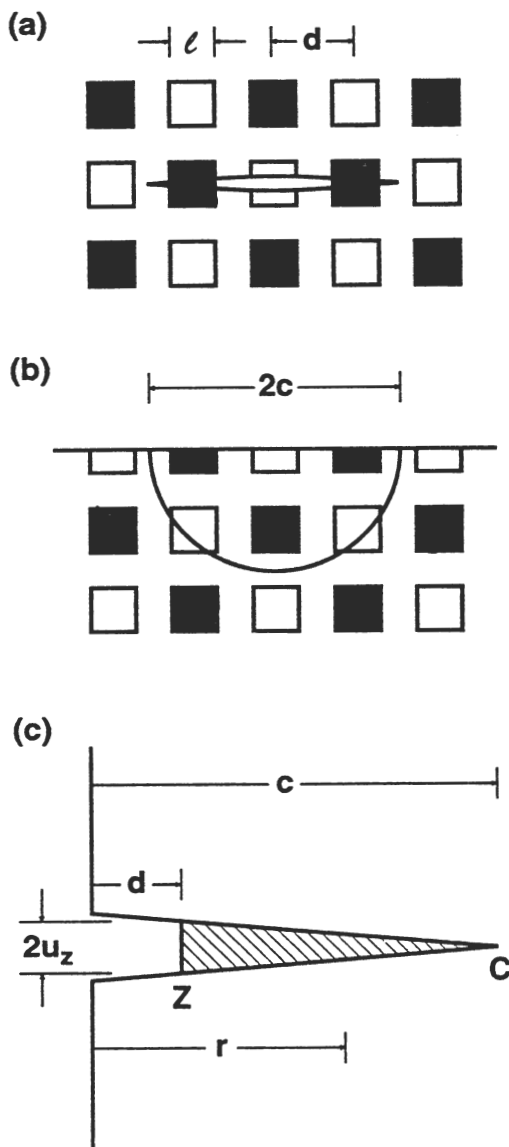
Figure 1. Microstructural model of grain bridging for penny crack in microstructure with bridging grains (squares): (a) in-plane view; (b) out-of-plane view. (c) Coordinate system for bridging zone. Crack initiates in residual tensile field at $c \leq d$, and thereafter extends into bridging field.

The toughening associated with the bridging is calculated according to crack-size domain, as follows [8,9,13,17]:

(i) **Small Cracks** ($c \leq d$), no bridge intersections. Within this region the crack experiences only the matrix tensile stress, $+\sigma_R$. Assuming this field to be uniform, we obtain

$$T_\mu(c) = -K_\mu(c) = -\psi \sigma_R c^{1/2} \tag{10}$$

where ψ is a geometry dependent coefficient. This K_μ term is not expected to be present in **straight** cracks, where tensile and compressive facets average to zero stress along the crack front.

(ii) **Intermediate Cracks** ($c \geq d$, $0 \leq u \leq u_\ell$), bridges intersected. There are two contributions to the toughness in this region, $T_\mu(c) = T_\mu'(c) + T_\mu''(c)$. The first is an opening post-intersection component from the persistent residual tensile stress field from (i) above,

$$T_\mu'(c) = -\psi \sigma_R c^{1/2} [1 - (1 - \alpha_d^2 \ell^2 / c^2)^{1/2}]. \tag{11}$$

The second is a countervailing closing component from the bridging tractions, Eq. 7. This contribution is most readily evaluated as a J-integral,

$$R_\mu''(u) = 2 \int_0^{u_z} p(u) du$$
$$= 2 p_M u_z (1 - u_z / \epsilon_\ell \ell). \tag{12}$$

The displacement $u_z = u_z(c)$ at the edge of the bridging zone (i.e. first bridge intersection at $c = d$, Fig. 1c) may be evaluated approximately from the Sneddon crack profile relation ("weak shielding" approximation)

$$u_z(c) = (\psi K_A / E') [(c^2 - \alpha_d^2 \ell^2)/c]^{1/2}. \tag{13}$$

The toughness $T_\mu''(c)$ may be determined from the crack resistance $R_\mu''(c)$ by eliminating G_A and K_A from Eqs. 2-5:

$$T_\mu''(c) = E'^{1/2} \{ [R_\mu''(c) + G_*]^{1/2} - G_*^{1/2} \}. \tag{14}$$

This relation is implicit in T_μ'', so Eqs. 3, 11-14 must be solved simultaneously.

(iii) **Long Cracks** ($c \gg d$, $u_z \geq u_\ell$), bridging zone now of constant size and translating with the advancing crack. In this limit, $T_\mu' \rightarrow 0$ and the steady-state toughening increment is evaluated from Eq. 14 with $R_\mu'' = p_M \epsilon_\ell \ell / 2$ from Eq. 12.

2.3   ENVIRONMENTALLY-ENHANCED KINETIC CRACK GROWTH

Environmentally-assisted "slow" crack growth in ceramics manifests
itself as a finite "lifetime" at sustained stress. The slow crack
growth is characterized by a crack velocity function, $v(K)$ or $v(G)$.
The fundamental form of the $v(G)$ function is [17]

$$v(G_*) = v_0 \sinh[(G_* - 2\gamma_{BE})/2\Gamma] \qquad (2\gamma_{BE} \leq G_* \leq 2\gamma_B) \qquad (15)$$

where γ_{BE} is the fracture surface energy in the presence of the
reactive environment, and v_0 and Γ are intercept and slope parameters.
This function has provision for a threshold at $G_* = 2\gamma_{BE}$, and dynamic
velocity at $G_* = 2\gamma_B$.
    Combining $v = dc/dt$ in Eq. 15 with the relations in Sects. 2.1 and
2.2 then yields a differential equation in $c(t)$ for any specified time-
dependent applied stress.

3. STRENGTH: INDENTATION FLAWS

Now let us examine the influence of the T-curve on strength properties.
We reemphasize that strength pertains specifically to cracks in the
intermediate-crack domain, i.e. to the rising portion of the T-curve.
To place this into proper context, we again point out that most
traditional toughness evaluations are made in long-crack specimens.
Later we shall address short-crack properties, viz. spontaneous
microcracking and wear.

3.1 INERT STRENGTH

The inert strength of a ceramic material is determined by the condition
for instability under essentially equilibrium conditions: $dK_*(c)/dc \geq$
0 at $K_*(c) = T_0$ in Eq. 2 or, alternatively, $dK_A(c)/dc \geq dT(c)/dc$ at
$K_A(c) = T(c)$ in Eq. 3 [14]. The latter defines the familiar "tangency"
construction for toughness curves. The form of K_a and K_r in Eq. 1 is
determined by the relevant testing geometry and flaw type.
    In this section we consider controlled indentation radial cracks
formed at contact load P and subsequently subjected to uniform tensile
stress σ_a:

$$K_r = \chi P/c^{3/2} \qquad (16a)$$
$$K_a = \psi\sigma_a c^{1/2} \qquad (16b)$$

with χ a parameter defining the intensity of the residual contact field
[22] and ψ as defined in Eq. 10. Indentation cracks enable one to
"calibrate" T-curve parameters with maximum efficiency and, moreover,
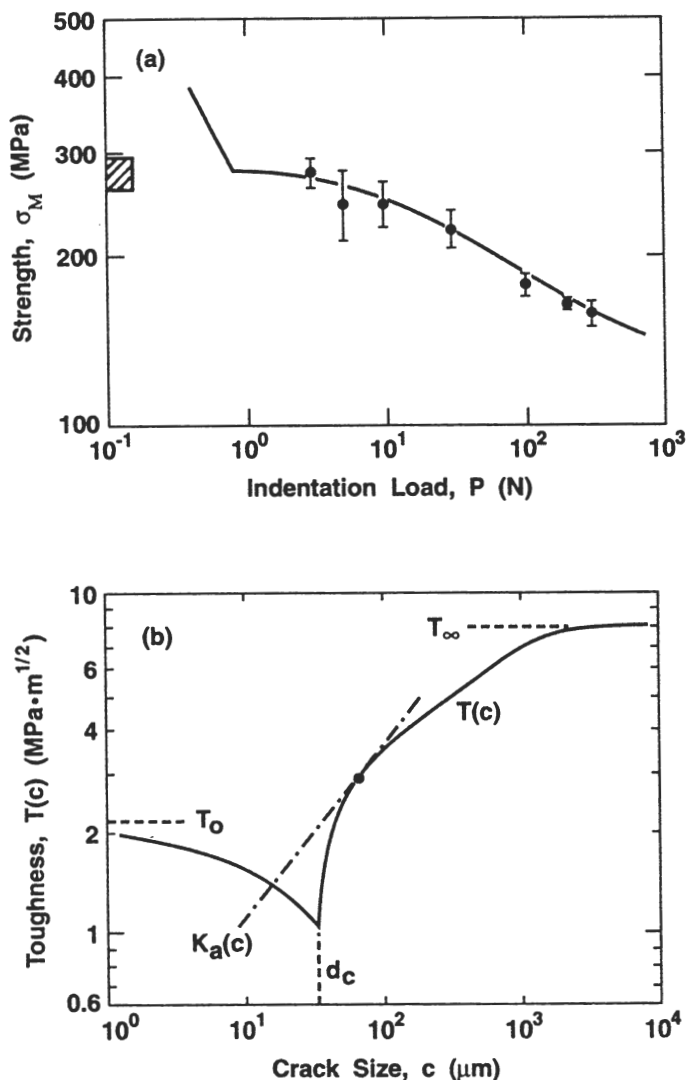take us close to the crack-size realm of natural flaws [12,13,23].

Figure 2. (a) Inert strength as function of Vickers indentation load for a reference single-phase polycrystalline alumina, grain size $\ell = 23$ μm, tested in dry silicone oil. Shaded region at left represents breaks from natural flaws. Solid curve is fit of bridging T-curve formalism. (b) Deconvoluted T-curve. Dashed line is $K_a(c)$ tangency condition for failure from **natural** flaw ($\chi = 0$).

Fig. 2a shows inert strength vs indentation load data for a "reference" alumina with single phase and equiaxed microstructure, grain size $\ell = 23$ μm. We note the strong tendency to a plateau at low P. These data reflect the quality of flaw tolerance alluded to earlier. The solid curve is a data fit obtained by adjusting the microstructural parameters μ, σ_R, ϵ_ℓ and α terms in Eq. 8, using a numerical algorithm [13,17]. From this fit we deconvolute the T-curve shown in Fig. 2b, using Eqs. 10-14. Note that the intrinsic material toughness initially diminishes from $T = T_0$ with crack size, due to the action of the residual tensile field at $c \leq d$ (Fig. 1). After the first bridge intersection the toughness rises sharply as a result of dominant frictional restraining stresses from the grain pullout. This rise continues as the bridging zone expands with crack extension, until the first bridge ultimately ruptures. At this point the bridging zone translates with the crack, and a steady state obtains at $T = T_\infty$.

The T-curve strongly stabilizes the crack growth en route to failure. For simplicity, consider a natural flaw without any residual stress ($\chi = 0$). Then $K_A = K_a \propto c^{1/2}$ in Eqs. 3, 16a. We show this applied loading function at the tangency condition in Fig. 2b. Suppose the initial size of the flaw lies to the right of the dashed line somewhere on the diminishing branch of the T-curve. Then at a certain point in the loading the flaw "pops in" and arrests on the rising branch of the T-curve. Further load is needed to extend the crack in stable equilibrium up the T-curve, until the configuration at $dK_A(c)/dc \geq dT(c)/dc$ is attained, whence the specimen fails. It is this precursor stability characteristic that is responsible for the flaw tolerance characteristic in Fig. 2a: the critical failure condition depends on the **final**, not the initial, flaw size.

The "calibrated" T-curve contains all the necessary ingredients to predict the effects of variations in microstructural characteristics on the toughness characteristics. We return to this prospect in Sect. 5.

3.2 RATE-DEPENDENT STRENGTH

Now let us consider the deleterious, rate-dependent influence of water-containing environments on strength, in accordance with the $v(G_*)$ velocity function of Eq. 15. We again focus on indentation flaws.

Strength data for the same alumina as in Fig. 2, but now tested in water at a fixed indentation load, are shown in Fig. 3 as a function of stressing rate. The solid curve through the data is a best fit from numerical solutions of the differential equation embodied in Eq. 15 for the time to grow the crack from its initial (stable) state to final instability, the "lifetime". This is done using the T-curve calibration from Sect. 3.1 and adjusting the crack velocity parameters v_0 and Γ [17]. Note the asymptotic limits: at fast stressing rates to the inert strength; at slow rates to a "fatigue limit".

This fitting procedure allows us to deconvolute velocity functions from the strength data. We plot the results from such deconvolutions in Fig. 4 [17]. The dashed curve at left represents the fundamental
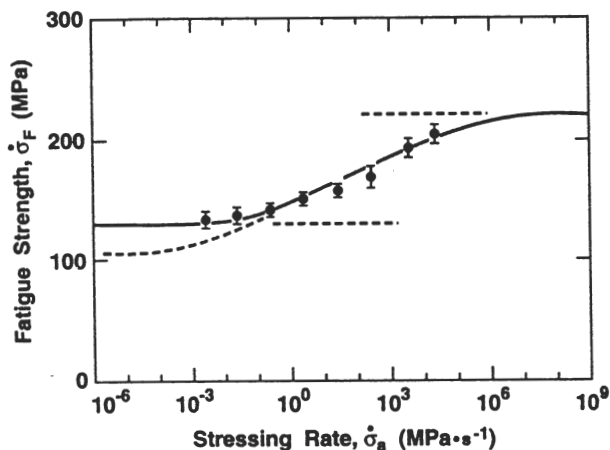
Figure 3. Strength of same alumina as Fig. 2, but as function of stressing rate for tests in water, Vickers indentations at P = 30 N. Upper horizontal line is inert strength limit from Fig. 2, lower line is fatigue limit. Dashed curve is equivalent response for hypothetical material without crack velocity threshold.
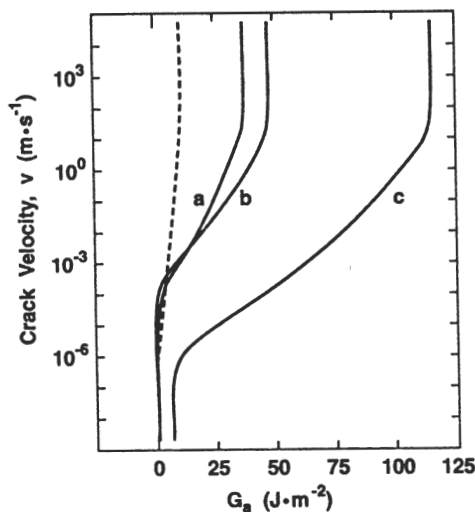

Figure 4. Velocity functions, deconvoluted from Fig. 3. Dashed curve is intrinsic, invariant crack-tip function, $v(G_*)$. Solid curves are history-dependent global functions $v(G_A)$, as monitored via the applied loading: (a) P = 3 N, $\dot{\sigma}_A = 10^3$ MPa·s^{-1}; (b) P = 30 N, $\dot{\sigma}_A = 10^3$ MPa·s^{-1}; (c) P = 30 N, $\dot{\sigma}_A = 10^{-1}$ MPa·s^{-1}.

v-G_* relation of Eq. 15, equivalent to the curve that a "global" observer at the load points would measure for a material with no shielding ($K_r = 0 = K_\mu$). The solid curves are the corresponding $v(G_A)$ curves for indentation flaws with shielding present. We see that the global velocity curve is **history dependent**, i.e. is a function of the residual contact field and stressing rate. The curves shift because the shielding contribution to the toughness is no longer a unique function of crack size, but depends also on the subcritical path [17]. Such curve shifts are regularly reported in the ceramics literature.

These results have a special relevance to fatigue. Many ceramics exhibit a static fatigue stress limit (analogous to the lower stress limit apparent in Fig. 3) below which the lifetime is effectively infinite. A fatigue limit is usually considered to be a direct manifestation of the crack velocity threshold, the crack-tip stress intensity below which all propagation ceases. But this is not the whole story. A strong T-curve **enhances** the fatigue limit, and can even generate an effective limit in materials with no detectable natural velocity threshold. To illustrate, we include as the dashed curve in Fig. 3 the computed strength vs stressing rate function for a hypothetical material with the same velocity function as our alumina but with its threshold shifted to zero G_*. A fatigue limit is still apparent, albeit at a somewhat reduced stress level. Mathematically, the existence of this limit is possible because the bridging closure term $-K_\mu$ can negate the effective applied loading term $K_A = K_a + K_r$ in Eq. 1, giving rise to a zero velocity state $K_* = 0 = G_*$ in Eq. 15.

3.3   CYCLIC FATIGUE

We have just referred to fatigue in static loading. Taking the metals literature as a guide, we might suspect some additional reduction in the fatigue limit in cyclic loading, due to some hysteresis in the crack-tip shielding. Specifically, we might anticipate mechanical degradation from deterioration of bridging ligaments in repeated loading.

Cyclic fatigue tests are most conveniently conducted with the indentation flaw configuration [18]. Results of such tests at two frequencies on alumina (this time on a coarser material than in Figs. 2 and 3) are shown in Fig. 5. Theoretical curves, obtained once more by solution of the crack velocity differential equation in Sect. 2 (but for the new grain size), exhibit a similar fatigue limit to that in Fig. 3. The data do appear to fall systematically below this predicted limit at long lifetimes, suggesting a real mechanical degradation of the microstructure.

The modest level of this degradation in Fig. 5 is not necessarily discouraging if one regards a million cycles as a reasonable service limit. Nevertheless, the potential exists for stronger effects in other configurations, e.g. long cracks and materials with more pronounced T-curves. For this reason it is proper that one should attempt to understand the underlying causes of the degradation.
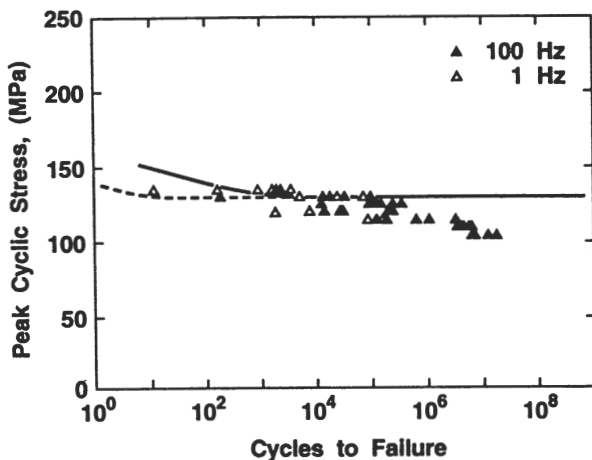
Figure 5. Cyclic fatigue plot for polycrystalline alumina, $\ell = 35$
μm, in water, Vickers indentations at $P = 30$ N, as function of
number of cycles. Open symbols are for 1 Hz, closed symbols 100
Hz. Curves are predictions for 1 Hz (dashed) and 100 Hz (solid)
assuming slow crack growth without mechanical degradation.

4. IN-SITU SCANNING ELECTRON MICROSCOPY OBSERVATIONS

4.1   OBSERVATIONS OF BRIDGE EVOLUTION

In situ observations of crack microstructure interactions using optical
microscopy have played a pivotal role in identifying grain bridging as
an important toughening mechanism in ceramics [7,10]. The development
of miniature straining devices for operation within the scanning
electron microscope (SEM) have opened the possibility for more detailed
observation and quantitative analysis of bridging mechanisms [20,21].
    Fig. 6 presents SEM surface views of a crack-interface bridging site
in an alumina, grain size $\ell = 11$ μm, at two stages in monotonic loading
[20]. The bridge has continued to evolve between the two stages,
during which the crack front has undergone an incremental extension of
≈ 600 μm. Persistent frictional contact points P and S are indicated.
In the interval between (a) and (b) secondary fractures have been
initiated in the bridging grain adjoining P by the frictional
tractions. During this same interval a single secondary fracture in
the large grain to the right of S has **closed** significantly, indicating
a falloff in the frictional tractions. This latter is indicative of a
tail-dominated constitutive stress-separation function, as assumed in
Eq. 7.
    Fig. 7 presents analogous views of a frictional site in the alumina
used in Fig. 5, at various stages of cyclic loading [18]. There is
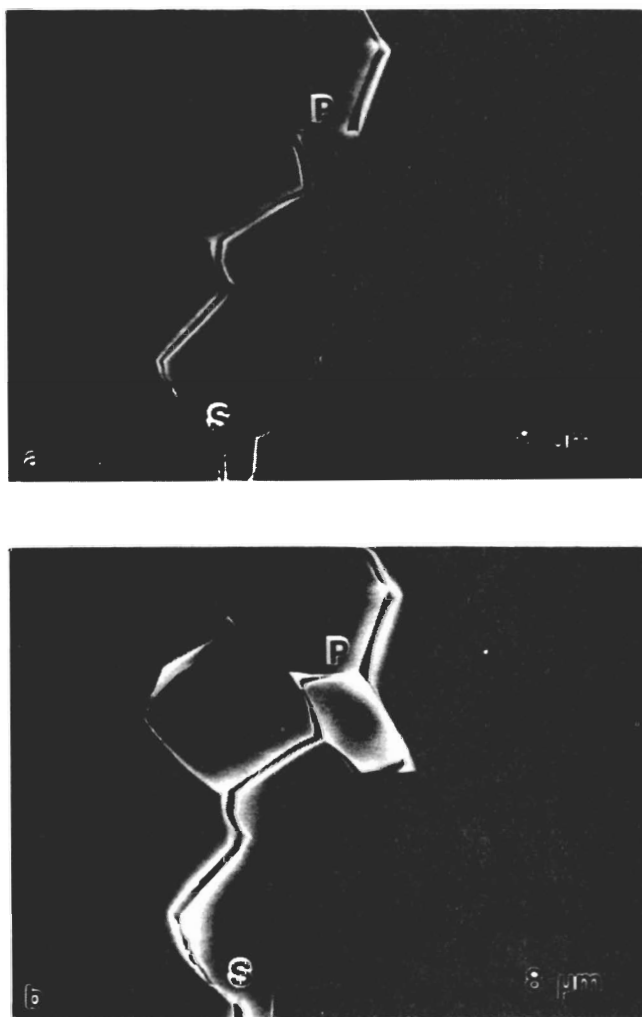gradual cumulation of debris from repeated load reversal at the sliding

Figure 6.   SEM micrographs showing evolution of grain-bridging
ligament at a crack interface in alumina, $\ell = 11$ μm, at distances
(a) 600 μm and (b) 1190 μm behind the advancing crack tip.   P and
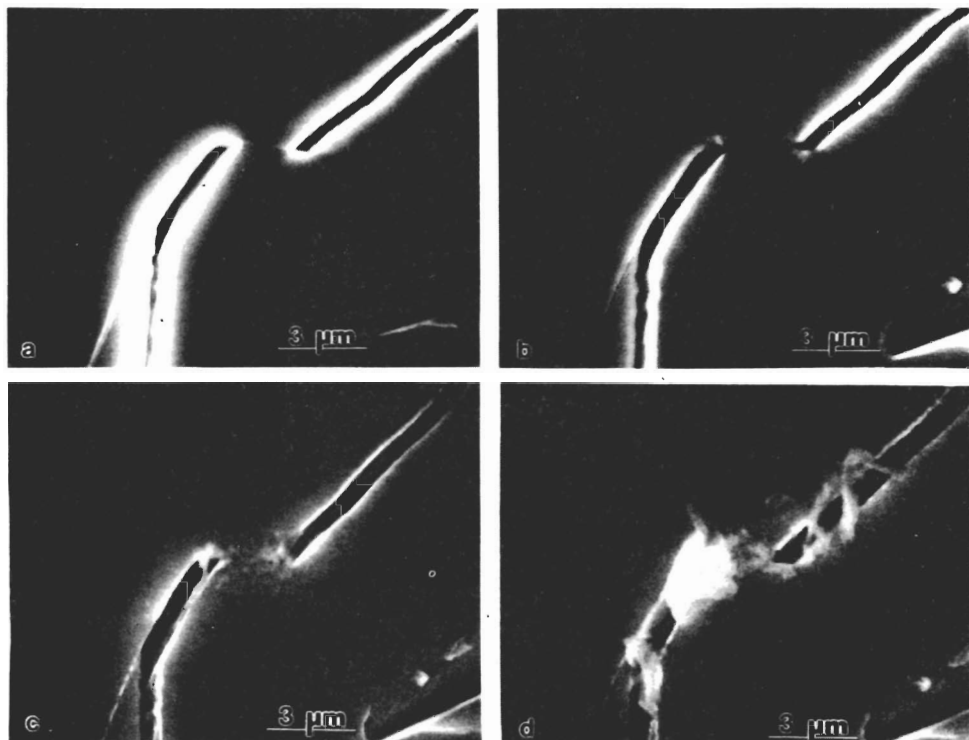S denote frictional contact points.

Figure 7. SEM micrographs of frictional grain facet in same alumina as Fig. 5, at various stages of cycling loading (vacuum, 2 Hz, unless otherwise indicated): (a) after initial propagation; (b) after 20000 cycles, with accompanying crack propagation 90 μm; (c) after 45000 cycles, no propagation; (d) after 50000 cycles (air, 10 Hz), propagation 20 μm. Note debris at friction facet.

grain facet, even between (b) and (c) where no primary crack growth occurs. Stage (d) shows strongly enhanced buildup of the debris after prolonged additional cycling in air. The debris may be taken as direct evidence for degradation of the interface at the sliding facet. Analysis using the bridging formulation in Sect. 2 indicates that the reduction in friction coefficient needed to account for the mechanical fatigue effect in Fig. 5 is modest, from $\mu = 1.8$ to 1.4 [18].

4.2   QUANTITATIVE CRACK PROFILE MEASUREMENTS

The quantitative capability afforded by the SEM is demonstrated in Fig. 8 with measurements of crack-opening displacement (COD) 2u as a function of distance x behind the crack tip, for the alumina in Fig. 6. The crack profile is seen to be closer to linear than the usual Irwin-parabola for stress-free walls [20], reflecting the closure effect of bridging tractions. In the limit of small bridging zones, as pertains to small extensions Δc from a long notch, the profile may be approximated by the Barenblatt relation

$$u(x) = (8x/\pi)^{1/2} K_A/E'$$
$$- (2/\pi E') \int_0^{\Delta c} p(x') \ln[(x'^{1/2} + x^{1/2})/(x'^{1/2} - x^{1/2})] dx' \quad (16)$$
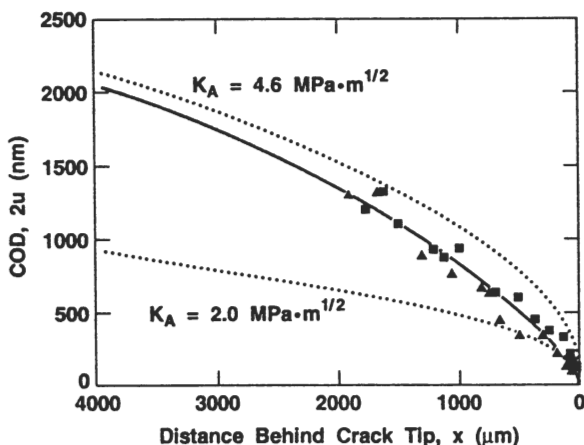

Figure 8. Measured crack-opening displacement at crack interface in same alumina as Fig. 6, compact-tension specimen, extended crack length $\Delta c = 1.9$ mm. Solid curve is fitted profile from Eq. 16. Dashed curves are enveloping Irwin parabolas for $K_A = 4.6$ $MPa \cdot m^{1/2}$ and $K_A = T_0 = 2.0$ $MPa \cdot m^{1/2}$.
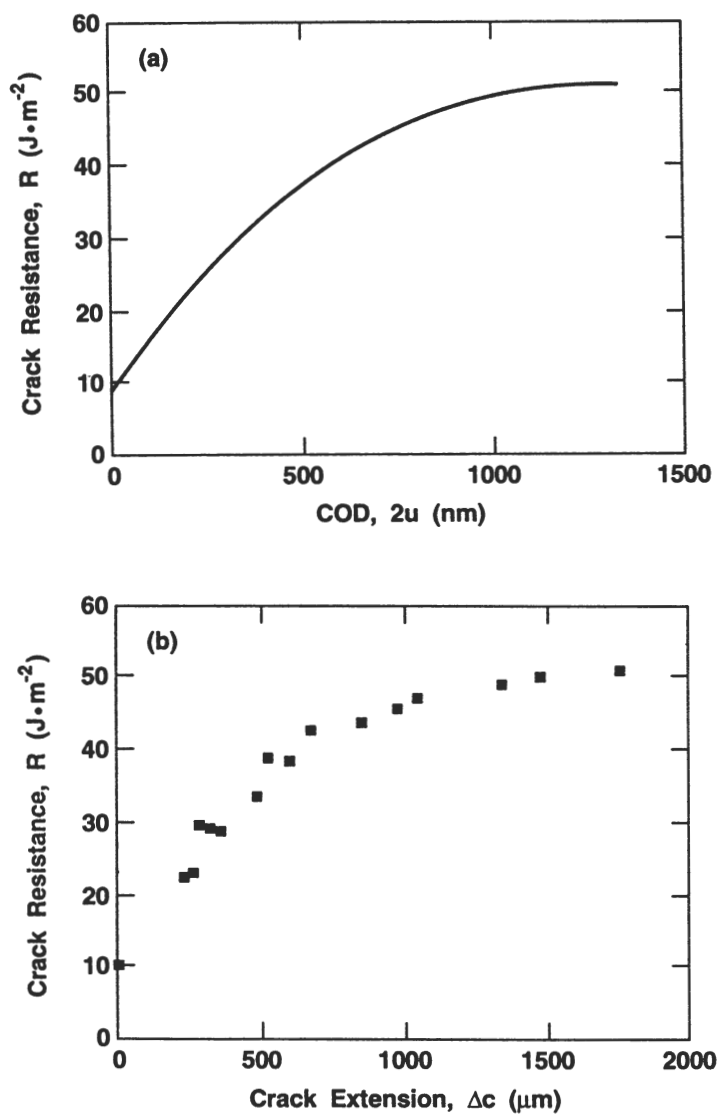
224

Figure 9. Crack-resistance curves corresponding to constitutive functions evaluated from crack profile in Fig. 8, (a) R(u), and (b) R(Δc).

with x now a field point at which the displacement is to be evaluated and x' a source point for the closure stresses. The problem is to find a solution for p(x'), thence p(u), self-consistent with the measured u(x). Eq. 16 is a nonlinear integral equation, for which there is no analytical solution. The solid curve in Fig. 8 is a best fit obtained by numerical iteration.

Once p(u) is known the crack-resistance curves are readily evaluated using the J-integral in Eq. 12 (recall that the contribution from Eq. 10 is negligible for straight cracks), identifying $2u_z$ with the notch-tip COD. The resulting R(u) curve for the alumina is shown in Fig. 9a. We assert that R(u) is a material property, since it is uniquely dependent on the intrinsic function p(u). On the other hand, the corresponding R(Δc) curve in Fig. 9b, evaluated in conjunction with the geometry-sensitive profile u(Δc), is a function of test configuration.

5. MICROSTRUCTURAL CONTROL OF TOUGHNESS PROPERTIES

We have indicated the strong influence of microstructural variables on toughness-curve characteristics, and the associated potential for manipulating mechanical properties through controlled processing. Two examples serve to illustrate the point:

5.1 GRAIN-SIZE EFFECTS

The role of grain size on the strength characteristics of alumina has been systematically investigated in an indentation-strength study [15]. Fig. 10a plots indentation-strength data for selected grain sizes. The solid curves correspond to predictions from the calibrated bridging theory from Sect. 3. Fig. 10b plots the deconvoluted T-curves. Observe the effect of coarsening the microstructure: the strengths tend to more pronounced, low-load plateaus, hence greater flaw tolerance; reductions of strength and toughness in the short-crack domain are compensated by increases in the long-crack domain.

The bridging model also provides insights into the nature of flaw states in strength-grain size characteristics. Fig. 11 is an "Orowan-Petch" plot of strength data for failures from natural flaws ($K_r = 0$) in our aluminas as a function of inverse square-root grain size [15]. Included as the solid and dashed curves are the predicted responses for intrinsic (processing) grain-facet flaws ($c_f \approx d = \alpha_d \ell$) and extrinsic (surface) flaws (c_f specified). Note that the solid and dashed curves merge in the large grain-size (Orowan) region. The insensitivity of the strength to any assumptions concerning type or initial size of flaw in this region indicates an instability condition controlled by material properties: failure is determined by a single point, the tangency point, on the T-curve. (We point out that the solid curve is not strictly linear in this region, as would obtain if ideal Griffith
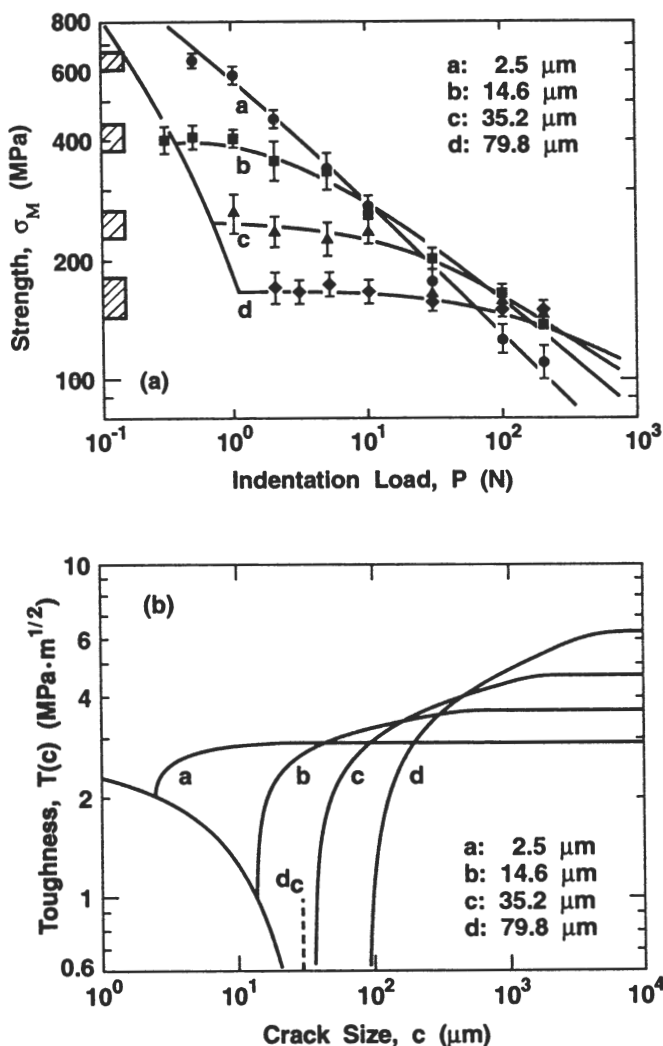
Figure 10. (a) Vickers indentation-strength data for four single-phase aluminas of differing grain size. Solid curves are predictions using calibrated bridging stress-intensity factor from Sect. 3. Note enhanced plateau behavior at larger grain sizes. Curves are theoretical fits from bridging model. (b) Corresponding deconvoluted T-curves. Vertical dashed line denotes intersection point of curve with crack-size axis at T = 0 for ℓ = 30 μm, corresponding to onset of spontaneous microcracking. Note tendency for curves to cross in both (a) and (b).
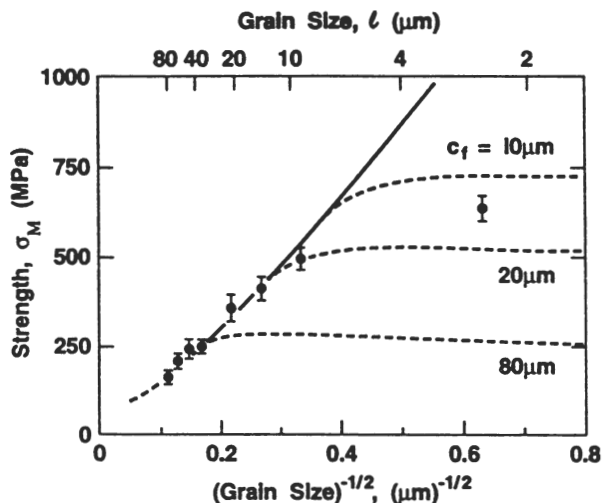
Figure 11. Strength versus inverse square-root grain size for alumina. Data are failures for polished, unindented specimens. Solid curve is prediction from bridging model for intrinsic flaws. Dashed curves are predictions for extrinsic flaws of specified initial size c_f. Note insensitivity of strength to flaw size in large grain-size domain.
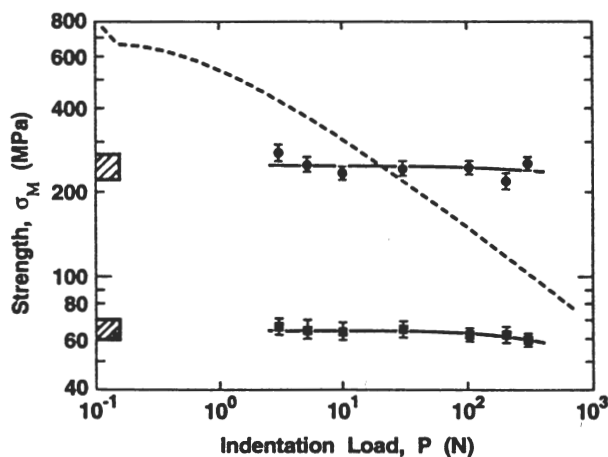

Figure 12. Inert strength as function of Vickers indentation load for an alumina matrix composite, grain size $\ell = 6$ μm, with 20 vol.% second-phase aluminum titanate particles. Lower data are for degraded material with $\ell = 14$ μm, above the critical grain size for spontaneous microcracking. Included as the dashed curve is prediction for equivalent monophase alumina ($\ell = 6$ μm).

behavior, i.e. flaw scaling with grain size, single-valued toughness T = T_0, were to prevail.) However, the curves diverge in the small grain-size (Petch) region, reflecting the sensitivity to flaw size usually associated with ceramics. On passing into this region the extrinsic flaws begin to dominate their microstructural counterparts, and traverse the tangency points on the T-curves (Fig. 10b) beyond which precursor stable crack growth prior to failure no longer occurs. Only one of the data points in Fig. 11, that of the finest grain size, appears to fall into the extrinsic region.

5.2   SECOND-PHASES

A second illustrative example demonstrates the importance of microstructural parameters other than grain size. We consider a model composite ceramic in which aluminum titanate has been added as a particulate second phase to an alumina matrix, grain size 6 μm [16]. Aluminum titanate was selected because of its unusually strong thermal expansion mismatch relative to alumina. An aging heat treatment promoting grain growth to ℓ = 14 μm caused general microcracking (see Sect. 6.1) in the composite.

Results of indentation-strength tests on the as-fabricated material are shown as the upper set of data points in Fig. 12. Included for comparison is a predicted curve for single-phase alumina of the same grain size (ℓ = 6 μm). It is immediately apparent that the composite has greatly exaggerated flaw tolerance relative to the alumina, although at the expense of short-crack strength. Also included is a data set for the heat-treated composite. The strength level for this latter material is severely reduced, as expected for an overaged microstructure.

A proper understanding of the bridging micromechanisms responsible for the striking changes in Fig. 12 is yet to be attained. Is the main role of the enhanced mismatch one of intensifying the frictional tractions at compressive bridging facets, or to enhance the formation of bridges by providing favorable tensile paths for deflection? In situ studies may help to provide answers. Once the micromechanisms are identified, the challenge will be to modify the model in Sect. 2.

These results demonstrate the capacity for improved strength properties in ceramic composites, particularly in the long-crack domain. Potential pitfalls in fabrication strategies are also apparent. The line between ultra-high toughness and unacceptable weakness may be very fine indeed.

6.   SHORT-CRACK PROPERTIES: SPONTANEOUS MICROCRACKING AND WEAR

What is good for properties that pertain to long or intermediate cracks may not be so for short cracks. The very ingredients responsible for

flaw tolerance, notably internal residual stresses, can be detrimental to general microcracking and wear resistance.

6.1   SPONTANEOUS MICROCRACKING

It is well known that noncubic polycrystals tend to general microcracking above a critical grain size. Such microcracking is attributable to the action of residual thermal expansion stresses. In terms of our shielding model, the critical condition is that processing flaws at tensile grain boundary facets should be unstable in the absence of any extraneous driving force. Seen from the perspective of Fig. 10b, a minimum requirement for such spontaneous instability is that the unstable branch of the toughness curve should intersect the abscissa ($K_A = T = 0$) at the flaw size c_f. Beyond this point instability ensues, and the microcrack arrests on the stable branch. Writing $c_f = \beta \ell$, with β a dimensionless constant (geometrical scaling), the critical grain size may be determined directly from Eq. 10 at equilibrium, $K_\mu(c) = \psi \sigma_R (\beta \ell_c)^{1/2} = T_0$:   thus [19]

$$\ell_c = (1/\beta \psi^2)(T_0/\sigma_R)^2 . \tag{17}$$

From Fig. 10b we estimate $\ell_c \approx 30$ μm for our alumina, which accords with experimental observations of spontaneous microcracking in the same series of aluminas [15]. Fig. 13 is a micrograph of an individual microcrack in a coarse-grained alumina.

6.2   MICROFRACTURE-WEAR PROCESSES

The earliest theories of surface removal by contact-induced cracking in brittle surfaces suggested that the least severe wear rates should occur in those materials with the highest toughness [24]. Such theories presume that the toughness is single-valued. The question arises as to the behavior in ceramics with strong T-curves.

Fig. 14 presents wear data on aluminas at three grain sizes [19]. Of these aluminas, the coarser have the higher conventional (long-crack) toughness. Yet it is the coarser aluminas here that show the greater susceptibility to wear degradation. Wear is quantified in Fig. 14 by the diameter of a scar generated by a rotating hard (Si_3N_4) sphere at specified contact time. The scar diameter increases monotonically with time for each material, initially slowly and subsequently, after an "incubation" period, abruptly. Whereas the initial increase is microstructure-invariant, the transition shifts to smaller times at the larger grain sizes.

Hence the "toughest" aluminas exhibit the most rapid degradation. A qualitative resolution to the apparent anomaly is once more to be found in the T-curve construction of Fig. 10b. The coarser microstructures indeed show greater long-crack toughness. However, it is the short-crack domain that is relevant to wear; and, as we have
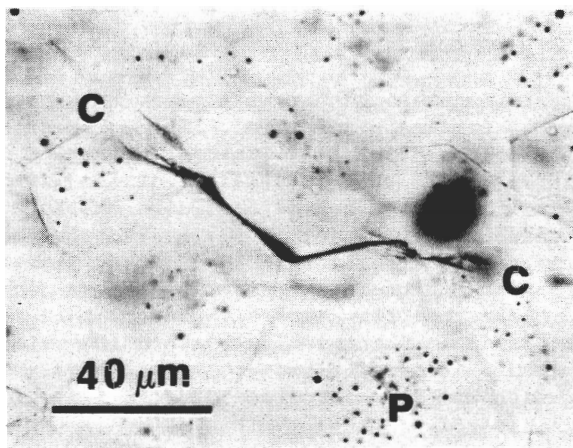
Figure 13. Optical micrograph showing extended microcrack (C-C) in
alumina, $\ell = 80$ μm. Note that, contrary to "conventional
wisdom", grain-size microcracks are quite visible, here in
transmitted light, by virtue of residual opening associated with
release of internal tensile stress. Some processing pores (P)
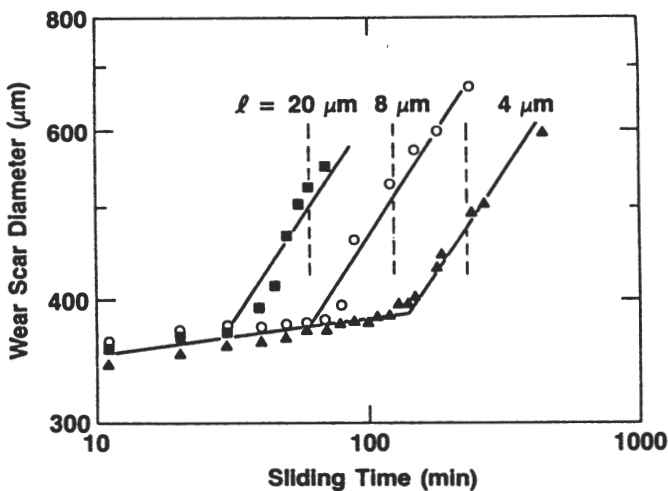are also visible.

Figure 14. Wear data for aluminas at three grain sizes. Note
initially slow increase of scar diameter, abrupt transition to
severe microfracture-controlled wear after critical sliding time.
Transition time diminishes at increasing grain size.

remarked before, the T-curves cross each other.

Microscopy reveals the initial wear to be slight, with indications of dislocation activity [19]. The abrupt increase is marked by the sudden incidence of gross chipping and grain removal. The results may therefore be interpreted in terms of a deformation-fracture transition, in which tensile stresses σ_D from the deformation augment those from the thermal expansion anisotropy, i.e. $\sigma_R' = \sigma_R + \sigma_D$. Suppose that these deformation stresses cumulate monotonically with time, i.e. $\dot{\sigma}_D = \sigma_D/t = $ const. Then replacing σ_R by σ_R' in Eq. 17 allows us to solve for the time to induce microcracking [19]

$$t_* = (\sigma_R/\dot{\sigma}_D)[(\ell_C/\ell)^2 - 1] \qquad (\ell \leq \ell_C). \qquad (18)$$

Observe that $t_* = 0$ at $\ell = \ell_C$, as required. As ℓ decreases below ℓ_C, t_* diminishes, in qualitative accord with observation. The shifts in Fig. 14 are quantitatively consistent with a stress cumulation rate $\dot{\sigma}_D = 5$ MPa·s^{-1}.

The implications concerning optimization of microstructures for maximum resistance to spontaneous microcracking and microfracture-induced wear are clear in this case - refine the grain size and, if possible, avoid internal residual stresses. It is reiterated that such measures may run entirely counter to the requirements for maximum large-crack toughness and flaw tolerance.

CONCLUSIONS

We have described toughness-curve phenomena in terms of a grain-interlocking bridging model. Essential microstructural ingredients for strong T-curves are weak boundaries, high internal stresses, and coarse grains. Our model has been illustrated with data from alumina, but a wider applicability to ceramics in general is asserted.

The T-curve has positive implications in strength. These include flaw tolerance and an enhanced fatigue limit. However, such benefits could be countered to some extent by possible bridge degradation in cyclic loading.

In situ observations of bridging sites in the scanning electron microscope provide insight into the degradation micromechanisms, and allow for quantitative evaluation of the crack-interface tractions.

Short-crack properties, spontaneous microcracking and abrasive wear, may be exacerbated in materials with strong T-curves.

ACKNOWLEDGEMENTS

REFERENCES

[1] H. Hübner and W. Jillek (1977) "Sub-Critical Crack Extension and Crack Resistance in Polycrystalline Alumina", J. Mater. Sci. **12** 117-25.

[2] R. Knehans and R.W. Steinbrech (1982) "Memory Effect of Crack Resistance During Slow Crack Growth in Notched Al_2O_3 Bend Specimens", J. Mater. Sci. Lett. 1 327-29.

[3] R.W. Steinbrech, R. Knehans and W. Schaarwächter (1983) "Increase of Crack Resistance During Slow Crack Growth in Al_2O_3 Bend Specimens", J. Mater. Sci. **18** 265-70.

[4] R. Knehans and R.W. Steinbrech (1984) "Effect of Grain Size on the Crack Resistance Curves of Al_2O_3 Bend Specimens"; in **Science of Ceramics**, Vol. 12, pp. 613-19, ed. P. Vincenzini. Ceramurgia, Imola, Italy.

[5] R.F. Cook, B.R. Lawn and C.J. Fairbanks (1985) "Microstructure-Strength Properties in Ceramics: I. Effect of Crack Size on Toughness", J. Am. Ceram. Soc. **68** 604-15.

[6] M.V. Swain (1986) "R-Curve Behavior in a Polycrystalline Alumina Material", J. Mater. Sci. Let. 5 1313-15.

[7] P.L. Swanson, C.J. Fairbanks, B.R. Lawn, Y-W Mai and B.J. Hockey (1987) "Crack-Interface Grain Bridging as a Fracture Resistance Mechanism in Ceramics: I. Experimental Study on Alumina", J. Am Ceram. Soc. **70** 279-89.

[8] Y-W. Mai and B.R. Lawn (1987) "Crack-Interface Grain Bridging as a Fracture Resistance Mechanism in Ceramics: II. Theoretical Fracture Mechanics Model", J. Am. Ceram. Soc. **70** 289-94.

[9] R.F. Cook, C.J. Fairbanks, B.R. Lawn and Y-W. Mai (1987) "Crack Resistance by Interfacial Bridging: Its Role in Determining Strength Characteristics", J. Mater. Research **2** 345-56.

[10] P.L. Swanson (1988) "Crack-Interface Traction: A Fracture-Resistance Mechanism in Brittle Polycrystals"; in **Advances in Ceramics**, Vol. 22, pp. 135-55, Fractography of Glasses and Ceramics. American Ceramic Society, Columbus, OH.

[11] R.W. Steinbrech and O. Schmenkel (1988) "Crack-Resistance Curves of Surface Cracks in Alumina", J. Am. Ceram. Soc. 71 C271-73.

[12] S.J. Bennison and B.R. Lawn (1989) "Flaw Tolerance in Ceramics With Rising Crack-Resistance Characteristics" J. Mater. Sci. 24 3169-75.

[13] S.J. Bennison and B.R. Lawn (1989) "Role of Interfacial Grain-Bridging Sliding Friction in the Crack-Resistance and Strength Properties of Nontransforming Ceramics", Acta Metall. 37 2659-71.

[14] Y-W. Mai and B.R. Lawn (1986) "Crack Stability and Toughness Characteristics in Brittle Materials", Ann. Rev. Mat. Sci. 16 415-39.

[15] P. Chantikul, S.J. Bennison and B.R. Lawn (1990) "Role of Grain Size in the Strength and R-Curve Properties of Alumina," J. Am. Ceram. Soc., 73 2419-27.

[16] J.L. Runyan and S.J. Bennison, "Fabrication of Flaw-Tolerant Aluminum-Titanate-Reinforced Alumina", J. Europ. Ceram. Soc., in press.

[17] S. Lathabai and B.R. Lawn (1989) "Fatigue Limits in Noncyclic Loading of Ceramics with Crack-Resistance Curves", J. Mat. Sci. 24 4298-4306.

[18] S. Lathabai, J. Rödel and B.R. Lawn, "Cyclic Fatigue from Frictional Degradation at Bridging Grains in Alumina", J. Mater. Sci., in press.

[19] S-J. Cho, B.J. Hockey, B.R. Lawn and S.J. Bennison (1989) "Grain-Size and R-Curve Effects in the Abrasive Wear of Alumina", J. Am. Ceram. Soc. 72 1249-52.

[20] J.Rödel, J.F. Kelly and B.R. Lawn, "In Situ Measurements of Bridged Crack Interfaces in the SEM", J. Am. Ceram. Soc., in press.

[21] J. Rödel, J.F. Kelly, M.R. Stoudt and S.J. Bennison, "A Loading Device for Fracture Testing of Compact Tension Specimens in the SEM," Scanning Microscopy, in press.

[22] B.R. Lawn, A.G. Evans and D.B. Marshall (1980) "Elastic/Plastic Indentation Damage in Ceramics: The Median/Radial Crack System", J. Am. Ceram. Soc. 63 574-81.

[23] B.R. Lawn, D.B. Marshall, P. Chantikul and G.R. Anstis (1980) "Indentation Fracture: Applications in the Assessment of Strength of Ceramics", J. Aust. Ceram. Soc. 16 4-9.

[24] A.W. Ruff and S.M. Wiederhorn (1979) "Erosion by Solid Particle Impact", in Treatise on Materials Science and Technology, Vol. 16, pp. 69-126, ed. C.M. Preece. Academic, New York.